VI International Conference on Particle-based Methods – Fundamentals and Applications
PARTICLES 2019
E. Oñate, M. Bischoff, D.R.J. Owen, P. Wriggers & T. Zohdi (Eds)

SIMULATION OF GEOLOGICAL FAULTS WITH DISCRETE ELEMENT METHOD

VADIM V. LISITSA[1,2], VLADIMIR A. TCHEVERDA[2] AND DMITRY R. KOLUYKHIN[2]

[1] Sobolev Institute of Mathematics SB RAS
4 Koptug ave., Novosibirsk, Russia, 630090
lisitsavv@ipgg.sbras.ru

[2] Institute of Petroleum Geology and Geophysics SB RAS
3 Koptug ave., Novosibirsk, Russia, 630090
cheverdava@ipgg.sbras.ru

Key words: DEM, Geological Faults

Abstract. We present an algorithm for simulation of the Earth's crust tectonic movements and formation of the geological faults and near-fault damage zones. The algorithms are based on the Discrete Elements Method, and it is implemented using CUDA technology. We used to simulate faults formation due to different scenarios of tectonic movements. We considered the displacements with dipping angles varied from 30 to 90 degrees; i.e., up to vertical throw. For each scenario, we performed simulations for some statistical realizations. To characterize the simulated faults and damage zones, we consider the strains distribution and apply data clustering and Karhunen-Loeve analysis to distinguish between different forms of the fault zones. In particular, clustering analysis shows that displacements with high and low dip angles form completely different geological structures. Nearly vertical displacements, high dip angles, form wide V-shaped deformation zones, whereas the at displacements cause narrow fault-cores with rapidly decreasing strains apart from the fault core. Results of the presented simulations can be used to estimate mechanical and seismic properties of rocks in the vicinity of the faults and applied further to construct models for seismic modeling and interpretation, hydrodynamical simulations, history of matching simulation, etc.

1 INTRODUCTION

A typical interpretation of geological faults from seismic data is a planar surface where the signal phase is discontinuous. Further on this representation of the faults is used in geological modeling to construct a model of the Earth's crust. As the result, faults are considered as a structural discontinuities in a model, whereas studies of the outcrops show that the faults and near-fault damage zones have more complex structure [1], [2]. In particular, damage zone may be highly fractured, thus, permeable especially for carbonates

[3], or it can be an impermeable due to the presence of deformation bonds which is typical for the sandstones [4]. Such differences of the local permeability near faults may strongly affect the reservoir performance. Thus a detailed representation of the fault and damage zone is required for efficient oil and gas exploration.

To study the fault formation due to tectonic motions, we suggest using numerical simulation. Simulation of finite deformations in solids and, in particular, in the geomaterials, geostructures, core samples, and Earth's crust can be done by either grid-based methods such as finite differences [5], finite elements [6], boundary elements [7] or by meshless approaches also known as discrete elements method (DEM) [8], [9]. The letter is preferred because no predefined crack or fault geometry is needed for simulation. However, particle-based methods are more computationally intense and require calibration of the particle properties to match the mechanics of the whole body [9], [10]. Despite this, the particle-based methods are incredibly flexible and can be used to generate multiple statistical realizations of the fault zones and study statistical features of the strongly deformed and highly-distorted zones. This opens a possibility to analyze the correlations between the peculiarities in the fault structure and their responses to the seismic waves. Moreover, use of the graphical processor units (GPU) significantly reduces the computational time making the DEM simulations an efficient and flexible tool.

In our opinion, meshless methods of geological faults formation simulations can be used to generate faults geometries in realistic environments. After that simulated faults can be introduced in geological models which are used for seismic modeling and imaging [11], [12], [13], moreover use advanced simulation techniques such as local mesh refinement [14], [15] allow studying seismic responses of the fine structure of near-fault damage zones.

The paper has the following structure. In the section 2, we describe the discrete element method, discuss its features, and present the algorithm for fault formation simulation by DEM. Description of the numerical experiments, cluster analysis, and statistical Karhunen–Loeve analysis is provided in section 3.

2 DISCRETE ELEMENT FORMULATION

To simulate the tectonic movements causing finite deformations and geological fault formation in the Earth's crust we use the discrete element method, following [16], [17], [18]. In this approach, the media is represented as an assembly of individual particles with a particular geometry and physical properties. Each particle is characterized by the coordinate of its center $\vec{x}^j$, radius R_j, repulsion and attraction bulk moduli K_r^+ and K_r^- respectively, tangential sliding stiffness K_s, and two friction coefficients μ_s is the static one and μ_d is the dynamic friction coefficient. Having set these parameters, one may define the interaction forces between two adjoint particles.

2.1 Computation of forces

Consider two particles with the numbers i and j, with the coordinates $\vec{x}^i$ and $\vec{x}^j$ and radii R^i and R^j respectively. Particle j acts on particle i with the normal elastic forces:

$$\vec{F}_n^{ji} = \begin{cases} K_r^-(R^i + R^j - \|\vec{X}^{ji}\|)\vec{n}^{ji}, & R^i + R^j - \|\vec{X}^{ji}\| > 0, \quad repulsion, \\ K_r^+(R^i + R^j - \|\vec{X}^{ji}\|)\vec{n}^{ji}, & 0 \le R^i + R^j - \|\vec{X}^{ji}\| \le r_0, \quad active\ \ bond, \\ 0, & R^i + R^j - \|\vec{X}^{ji}\| > r_0, \quad no\ \ bond, \end{cases} \tag{1}$$

where r_0 is the bond length, typically chosen equal to $0.05(R_i + R_j)$, vector $\vec{X}^{ji} = \vec{x}^i - \vec{x}^j$ connects the centers of the particles and directed from particle j to particle i, vector $\vec{n}^{ji} = \vec{X}^{ji}/\|\vec{X}^{ji}\|$ is the unit vector directed from the centers of particle j to the center of particle i or normal vector, because it is normal to the contact plane. Note, that we use the model of linear elastic particles interaction and assume that the repulsion and attraction bulk moduli coincide, which is mainly valid for geomaterials across a wide range of scales.

Additionally frictional forces are taken into account if two particles are in a contact [18]:

$$\vec{F}_t^{ji} = \begin{cases} -K_s\delta_t\vec{t}^{ji}, & K_s\delta_t \le \mu^s\|\vec{F}_n^{ji}\|, \quad static\ \ friction, \\ -\mu^d\|\vec{F}_n^{ji}\|\vec{t}^{ji}, & K_s\delta_t > \mu^s\|\vec{F}_n^{ji}\|, \quad dynamic\ \ friction, \end{cases} \tag{2}$$

where K_s is the tangential sliding stiffness, usually considered to be equal to bulk modulus; i.e., $K_s = K_r$, vector $\vec{t}^{ji}$ is the unitary tangential vector directed along the projection of the relative velocity onto the contact plane of two particles; i.e.,

$$\vec{t}^{ji} = \frac{\vec{v}^{ji} - (\vec{v}^{ji}, \vec{n}^{ji})\vec{n}^{ji}}{\|\vec{v}^{ji} - (\vec{v}^{ji}, \vec{n}^{ji})\vec{n}^{ji}\|}, \quad \vec{v}^{ji} = \vec{v}^i - \vec{v}^j. \tag{3}$$

In this notations $\vec{v}^{ji}$ is the relative velocity of the particle i with respect to particle j. Parameter δ^{ji} denotes the tangential displacement of the contact point from its initial position. Tangential forces provided by formula (2) satisfy the Coulombs law; i.e., the static friction governs the particles interaction if the forces as below a critical value. If the tangential forces exceed the critical dynamical friction proportional to normal force is applied. Typically the static friction is much higher than the dynamical one.

Additionally, an artificial dissipation is introduced in the system to prevent elastic waves from propagating through the model and ensuring the media to remain stable at infinite instants:

$$\vec{F}_d^i = -\nu\vec{v}^i, \tag{4}$$

where ν is an artificial viscosity.

The Earth's crust also remains under gravitational forces which are accounted as

$$\vec{F}_g^i = M_i g\vec{e}_3, \tag{5}$$

where $g = 9.8$ m/s is the gravitational constant, $\vec{e}_3 = (0, 0, 1)^T$, and M_i is the mass of the considered particle.

To compute the total forces acting at a particle one need to account the forces due to interactions with all the neighbors, plus artificial dissipation, plus gravitational forces, as a result, one gets:

$$\vec{F}^i = \sum_{j \in J(i)} \left[\vec{F}_n^{ji} + \vec{F}_t^{ji} \right] + \vec{F}_d^i + \vec{F}_g^i, \tag{6}$$

where $J(i)$ is the set of indexes of the neighbors of i-th particle.

2.2 Time integration

Having computed all external forces acting at j-th particle one may recompute its position using classical mechanics principles:

$$M^i \frac{d^2 \vec{x}^i}{dt^2} = \vec{F}^i \left(t, \vec{x}^i, \vec{x}^j, \frac{d\vec{x}^i}{dt}, \frac{d\vec{x}^j}{dt} \right), \tag{7}$$

where dissipative $\vec{F}_d^i$ and frictional forces $\vec{F}_t^{ji}$ explicitly depend on the particles velocities $\vec{v}^i = \frac{d\vec{x}^i}{dt}$.

To numerically resolve system of equations (7) we use the Verlet-like scheme with the velocity half-step [17], [19]. Assume coordinates, velocities, and thus forces of all particles are known at instant $t = t^n = \tau \cdot n$, then they can be updated to the instant t^{n+1} by the rule:

$$\begin{array}{l} \frac{(\vec{v}^i)^{n+1/2} - (\vec{v}^i)^n}{\tau/2} = \frac{1}{M^i} \vec{F}^i \left(t^n, (\vec{x}^i)^n, (\vec{x}^j)^n, (\vec{v}^i)^n, (\vec{v}^j)^n \right), \\ \frac{(\vec{x}^i)^{n+1} - (\vec{x}^i)^n}{\tau} = (\vec{v}^i)^{n+1/2}, \\ \frac{(\vec{v}^i)^{n+1} - (\vec{v}^i)^{n+1/2}}{\tau/2} = \frac{1}{M^i} \vec{F}^i \left(t^{n+1}, (\vec{x}^i)^{n+1}, (\vec{x}^j)^{n+1}, (\vec{v}^i)^{n+1/2}, (\vec{v}^j)^{n+1/2} \right), \\ j \in J(i). \end{array} \tag{8}$$

In case of no explicit dependence of forces on the velocities the scheme is the second order accurate, however if applied to the equation of motion for DEM, this scheme possesses only the first order of approximation.

To ensure the stability of the finite-difference scheme we use the time step as suggested in [17], [19]

$$\tau \leq 0.2 \frac{D_{min}}{V_{max}}, \tag{9}$$

where R_{min} is the minimum diameter of the particles, and V_{max} is the maximal velocity of perturbation propagation in the system. In the case on no artificial viscosity, the maximal velocity is the wave-speed of the longitudinal wave in the media, where the normal stresses and strains are related as $\sigma_{nn} = K_r \varepsilon_{nn}$, where K_r is exactly the attractions/repulsion bulk modulus used in the simulation. If there is a nontrivial artificial viscosity, the velocity will increase, however, this effect is compensated by the constant 0.2. The discussion can be found in [18].

Note, that the implementation of the algorithm is based on the use of Graphic Processor Units with the help of domain decomposition to band limit the dependency matrix. Discussion of the implementation can be found in [20].

2.3 Boundary conditions

Proper implementation of the boundary conditions is a challenging task for the particles-based methods. In our research, we deal with two types of boundary conditions. First, we impose the rigid boundary condition; i.e., the surface Γ_s is fixed, or its movement is prescribed. Moreover, it is stiff; thus the particles cannot penetrate through it. Formally, this type of boundary condition can be stated as follows. Assume a boundary $\Gamma_s = \{\vec{x}|x_2 = x_2^B\}$. If a particle is close enough to the boundary; i.e., if for the j-th particle $|x_2^j - x_2^b| \leq R^j$, then $F_2^{jB} = K_r^-(R^j - |x_2^j - x_2^b|)$.

However, numerical implementation of this condition requires extra conditional operators. Thus it is worth implementing stiff-boundary as a series of particles, to make the simulation uniform either in the interior of the domain or near the boundary. To do so, we introduced the "boundary" particles with the same physical properties as those of the interior particles. However, we do not compute the forces acting on the "boundary" particles but allow the "boundary" particles to move according to a prescribed law. We specify the particular movement laws in the section 3.

The second type of the boundary conditions is $P_{over} = const$. This condition ensures the constant overburden pressure. Note that, condition P_{over} assumes that external forces act at the upper boundary of the domain $\Gamma_p(t)$ along the normal direction to the boundary. This boundary is flexible, and it evolves in time; thus, to impose the boundary condition we need to follow the elements which form the upper boundary. This can be done, for example, by computing Voronoi diagrams for upper elements. However, such procedures are computationally intense. To overcome this difficulty, we suggest using the flexible membrane at the upper boundary [21], [22]. The idea of the approach is to introduce a layer of discrete elements so that the membrane elements are affected only by the normal forces.

If two adjoint membrane elements are interacting

$$\vec{F}_n^{m,m\pm1} = K_r(R^{m\pm1} + R^m - \|\vec{X}^{m,m\pm1}\|)\vec{n}^{m,m\pm1}, \tag{10}$$

if membrane element interacts with other elements

$$\vec{F}_n^{mi} = \ K_r(R^i + R^m - \|\vec{X}^{mi}\|)\vec{n}^{mi}, \quad R^i + R^m - \|\vec{X}^{mi}\| > 0. \tag{11}$$

It means that the adjoint membrane elements are bonded, and these bonds never bake, however no bonds of friction are considered when membrane elements interact with elements of other types. The membrane elements are ordered; thus it is easy to approximate constant pressure condition. If a membrane element with number m is considered then additional force, due to the pressure is

$$\vec{F}_p^m = 2PR^m\vec{n}, \tag{12}$$

where $\vec{n}$ is the vector normal to the boundary, which can be computed as:

$$\vec{n} = (x_2^{m-1} - x_2^{m+1}, x_1^{m-1} - x_1^{m+1})^T,$$

the direction of the normal vector is defined uniquely due to the ordering of the membrane elements.

2.4 Output parameters

Numerous parameters can be obtained as a result of discrete elements simulations. If rock properties are studied using uniaxial and triaxial stress tests, then the primary attention is paid to the distribution of the braked bonds [23], [24], stresses, and normal forces distribution [25] However, at the scale of the geological bodies a reliable parameter to determine fault zones is the strains distribution [26], [16], [17], [27], [11]. These strains can be further translated to the changes of physical parameters of rocks using the experimental laboratory measurements.

To estimate the strains distribution one may compute the relative displacements elementwise, after that the strain tensor components can be computed and interpolated to a regular grid. A detailed discussion of the strains estimation can be found in [26].

3 NUMERICAL EXPERIMENTS

In this paper, we focus our attention on the effect of the direction and amplitude of tectonic movement on the geometry of the fault and damage zone. DEM-based simulations include uncertainties due to the particle's positions and radii distributions. It means that for each scenario of the tectonic movements we need to perform a series of numerical simulations for different statistical realizations of the particles geometry distribution.

In all the experiments presented below, we use the following set of parameters. The size of the computational domain is 4000 m in horizontal and 500 m in the vertical direction. The repulsion/attraction modulus is 16 GPa, and same value is used for the tangential sliding stiffness. The coefficient of static friction is 0.8, which is typical for the majority of geomaterials, whereas the dynamic friction coefficient is 0.3, which is close to that of sandstone and limestone. We consider the bonds length proportional to the radii of the adjoint particles; i.e., $r_0 = 0.05(R_j + R_i)$. We assume that the formation is buried at 3000 m; thus the overburden pressure of 10^7 Pa is applied at the top boundary of the model. The particles radii are homogeneously distributed from 1.25 to 2.5 m. So, the total number of elements is 390000.

We consider several scenarios of dipping normal tectonic movements with the dip angles equal to 90°, 75°, 60°, 45°, 30°. Maximal vertical displacement is 100 m.

For each tectonic movement we simulate ten statistical realizations of the particles distributions; thus, 10 simulations are performed for each scenario. Also, we computed extra 20 realizations for the most common movement scenario with the dip angle equal to 60°. Each simulation consists of two stages. First, the elements should be compacted under the overburden pressure and gravitational forces. This step takes about 60 % of the computational time. Second, the tectonic movements are applied. The total simulation time for one experiment (one realization) is about 8.7 hours by a single GPU (NVIDIA Tesla M 2090).

We provide the strains distribution for displacement with dip angle equal to 30°, 60°, 90° in figures 1-3. The main trend observed from the presented figures is that for big dip angles; i.e., for nearly vertical displacements no narrow fault cores are formed. When the dip angle gets smaller fault cores are formed (figure 1) and they are located within

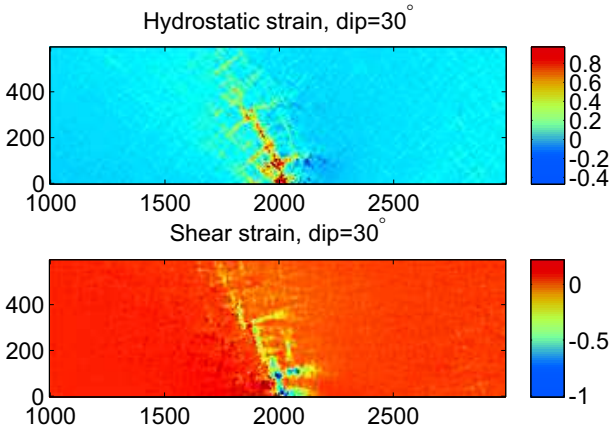

Figure 1: A single realizaton of hydrostatic (top) and shear (bottom) strains distribution in the fault zone for the displacement dip equal to 30°.

a narrow zone. Moreover, for low dip angles the form of the fault and its inclination is similar, thus might depend mainly on the medium properties rather than on the direction of tectonic movements. To verify this assumption, we perform clustering of the results and their statistical analysis in the following section.

3.1 Clustering of the results

According to the figures 1-3 fault zones formed after tectonic movements with low dip angles are similar. To quantify this observation, we applied k-means clustering of the computed strains distribution. Before processing to the formal analysis, we need to point out, that we performed two additional series of simulations (9 realizations in each series) corresponding to the tectonic movement dip angle equal to 60°. In total we have 27 statistical realizations corresponding to this scenario; however, we will still consider them as three independent series in our statistical analysis.

We start with the determination of the optimal number of clusters in which the data can be partitioned. To do so, we use the Calinski-Harabasz Index [28] which measures the ratio of the total inter-clusters variance to total within-cluster variance for all possible data subdivision. According to this criterion the optimal number of clusters is two. Then we applied k-means clustering technique to our data. We constructed clusters for each component of the strain tensor separately, as well as for all of them together. The panels in figure 4 represents the clustering results in two clusters. In these experiments we applied clustering to the all components of the strain tensor. One may note that the displacement scenarios with dip angles equal to 75° and 90° form one cluster, whereas all others form the second cluster. We consider the within-cluster sum of squares (WCSS); i.e., the functional which is minimized by the k-means algorithm:

$$D = \sum_{i=1}^{k} \sum_{e \in S_i} \| e - < e >_i \|,$$

where k is a number of clusters, S_i is the i-th cluster, a subset of the considered dataset,

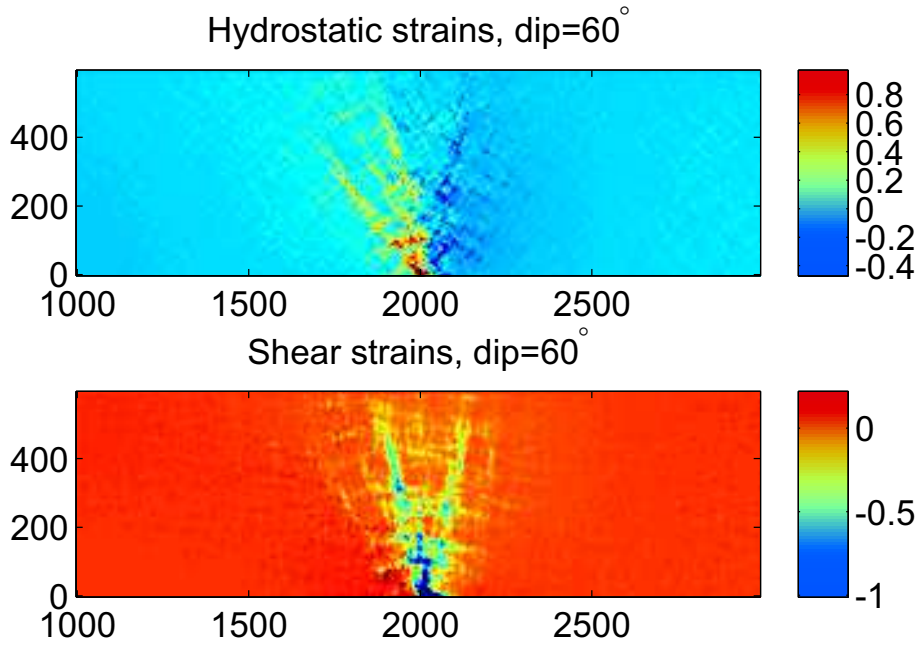

Figure 2: A single realizaton of hydrostatic (top) and shear (bottom) strains distribution in the fault zone for the displacement dip equal to 60°.

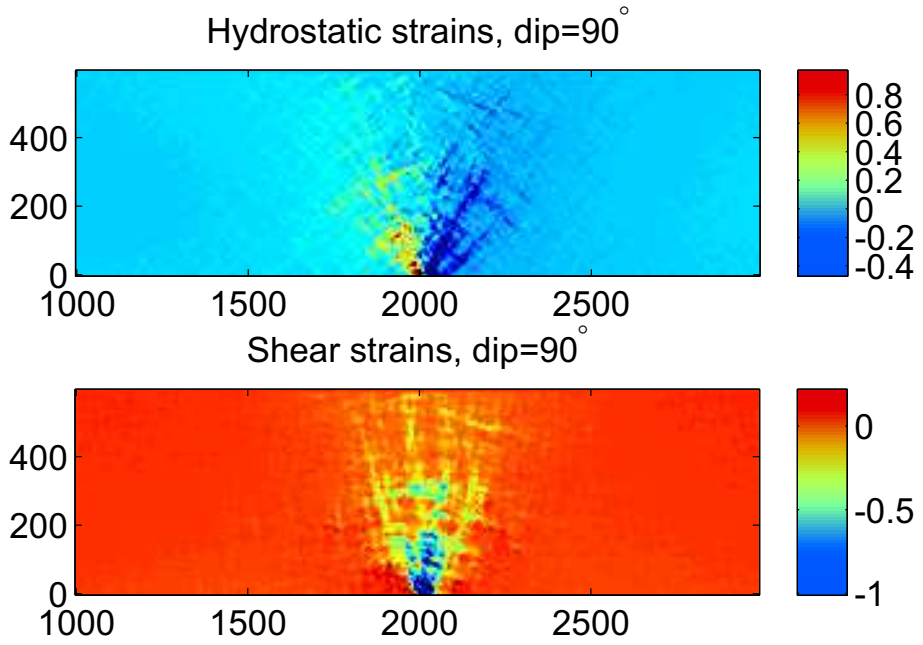

Figure 3: A single realizaton of hydrostatic (top) and shear (bottom) strains distribution in the fault zone for the displacement dip equal to 90°.

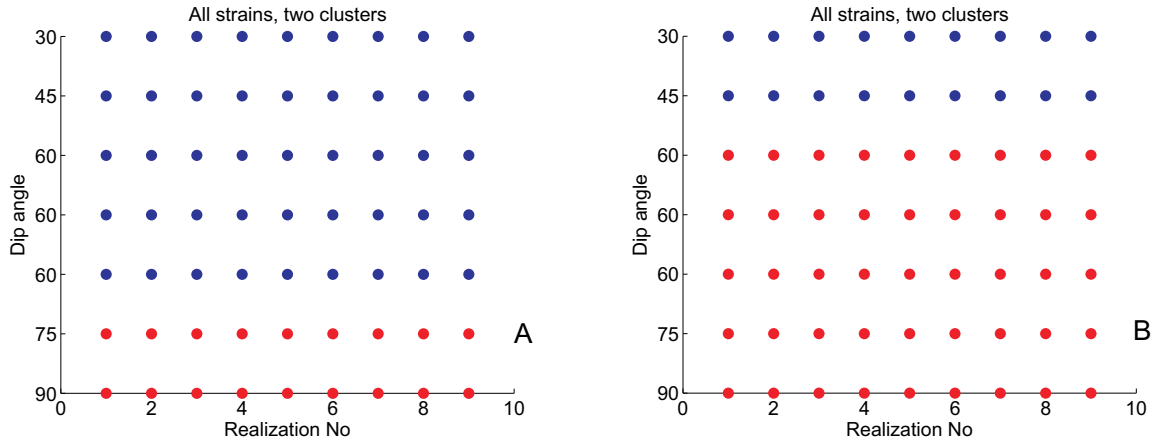

Figure 4: Panels representing data clustering (two clusters) for all components of strain tensor. Left panel (A) corresponds to the optimal clustering with minimal distance, right panel (B) represents a case of local minimum of k-means functional. Different colors correspond to different clusters.

$< e >_i$ is the mean value of the elements from i-th set S_i. There are different options to define the norm; however, in this work, we deal with the L^2 norm of vectors. So, the optimal clustering delivers $D_{all} = 3692$ respectively. However, there is another local minimum of the WCSS functional which leads to the clustering where strains for the tectonic displacements with dip angles equal to 30° and 45° form one cluster, whereas solutions corresponding to the subvertical movements go to the other cluster (figure 4 B). In the second case, the WCSS is $D_{all} = 3753$. The difference in the within-cluster distances between the two scenarios is less than 1%, and these two cases are hardly distinguishable. It means that the displacements with dipping angle equal to 60° can either form a wide deformation zone, same as subvertical displacements, or narrow inclined fault cores, same as in case of flat tectonic movements.

4 CONCLUSIONS

We presented an algorithm for simulation of the Earth's crust tectonic movements and formation of the geological faults and near-fault damage zones. The algorithms are based on the Discrete Elements Method, and it is implemented using CUDA technology. We used to simulate faults formation due to different scenarios of tectonic movements. We considered the displacements with dipping angles varied from 30 to 90 degrees; i.e., up to vertical throw. For each scenario, we performed simulations for some statistical realizations. To characterize the simulated faults and damage zones, we considered the strains distribution and applied data clustering to distinguish between different forms of the fault zones. In particular, clustering analysis shows that displacements with high (75° and 90°) and low (30° and 45°) dip angles form completely different geological structures. Nearly vertical displacements, high dip angles, form wide V-shaped deformation zones, whereas the flat displacements cause narrow fault-cores with rapidly decreasing strains apart from the fault core. Results of the presented simulations can be used to estimate mechanical and seismic properties of rocks in the vicinity of the faults and applied further

to construct models for seismic modeling and interpretation, hydrodynamical simulations, history of matching simulation, etc.

5 ACKNOWLEDGMENTS

The algorithm was developed by V. Lisitsa employed by IPGG SB RAS under support of Russian president grant MD 20.2019.5, numerical simulations were done by V. Lisitsa employed by IM SB RAS under support of RSCF grant no. 19-77-20004. V. Tcheverda did the geological interpretation of the results under support of the RSCF grant no. 17-17-01128, statistical analysis of the results was done by D. Kolyukhin under support of RFBR grant no. 18-05-00031. Simulations were done on the cluster NKS-30T+GPU of the Siberian supercomputer center under support of the RSCF grant no. 19-77-20004.

REFERENCES

[1] Choi J.-H., Edwards P., Ko K., and Kim Y.-S. Definition and classification of fault damage zones: A review and a new methodological approach. *Earth-Science Reviews.* (2016) **152**:70–87.

[2] Peacock D. C. P., Dimmen V., Rotevatn A., and Sanderson D. J. A broader classification of damage zones. *Journal of Structural Geology.* (2017) **102**:179–192.

[3] Hausegger S., Kurz W., Rabitsch R., Kiechl E., and Brosch F. J. Analysis of the internal structure of a carbonate damage zone: Implications for the mechanisms of fault breccia formation and fluid flow. *Journal of Structural Geology.* (2010) **32**:1349–1362.

[4] Fossen H., Schultz R. A., Shipton Z. K., and Mair K. Deformation bands in sandstone: a review. *Journal of the Geological Society.* (2007) **164**:755–769.

[5] González G., Gerbault M., Martinod J., Cembrano J., Carrizo D., Allmendinger R., and Espina J. Crack formation on top of propagating reverse faults of the Chuculay fault system, northern Chile: Insights from field data and numerical modelling. *Journal of Structural Geology.* (2008) **30**:791–808.

[6] Guiton M. L. E., Sassi W., Leroy Y. M., and Gauthier B. D. M. Mechanical constraints on the chronology of fracture activation in folded devonian sandstone of the western moroccan anti-atlas. *Journal of Structural Geology.* (2003) **25**:1317–1330.

[7] Resor P. G. and Pollard D. D. Reverse drag revisited: Why footwall deformation may be the key to inferring listric fault geometry. *Journal of Structural Geology.* (2012) **41**:98–109.

[8] Gray G. G., Morgan J. K., and Sanz P. F. Overview of continuum and particle dynamics methods for mechanical modeling of contractional geologic structures. *Journal of Structural Geology.* (2014) **59**(Supplement C):19–36.

[9] Lisjak A. and Grasselli G. A review of discrete modeling techniques for fracturing processes in discontinuous rock masses. *Journal of Rock Mechanics and Geotechnical Engineering.* (2014) **6**:301–314.

[10] Alassi T.H. and Holt R. Relating discrete element method parameters to rock properties using classical and micropolar elasticity theories. *International Journal for Numerical and Analytical Methods in Geomechanics.* (2012) **36**:1350–1367.

[11] Botter C., Cardozo N., Hardy S., Lecomte I., and Escalona A. From mechanical modeling to seismic imaging of faults: A synthetic workflow to study the impact of faults on seismic. *Marine and Petroleum Geology.* (2014) **57**:187–207.

[12] Kolyukhin D. R., Lisitsa V. V., Protasov M. I., Qu D., Reshetova G. V., Tveranger J., Tcheverda V. A., and Vishnevsky D. M. Seismic imaging and statistical analysis of fault facies models. *Interpretation* (2017) **5**:SP71–SP82.

[13] Vishnevsky D. M., Kolyukhin D. R., Lisitsa V. V., Protasov M. I., Reshetova G. V., Tcheverda V. A., Qu D., and Tveranger J. Correlation analysis of statistical facies fault models. *Doklady Earth Sciences.* (2017) **473**:477–481.

[14] Kostin V., Lisitsa V., Reshetova G., and Tcheverda V. Local time-space mesh refinement for simulation of elastic wave propagation in multi-scale media. *Journal of Computational Physics.* (2015) **281**:669–689.

[15] Lisitsa V., Reshetova G., and Tcheverda V. Finite-difference algorithm with local time-space grid refinement for simulation of waves. *Computational Geosciences.* (2012) **16**:39–54.

[16] Hardy S. and Finch E. Discrete-element modelling of detachment folding. *Basin Research.* (2005) **17**:507–520.

[17] Hardy S., McClayc K., and Munozb J. A. Deformation and fault activity in space and time in high-resolution numerical models of doubly Vergent thrust wedges. *Marine and Petroleum Geology.* (2009) **26**:232–248.

[18] Luding S. Introduction to discrete element methods. *European Journal of Environmental and Civil Engineering.* (2008) **12**:785–826.

[19] Mora P. and Place D. Simulation of the frictional stick-slip instability. *Pure and Applied Geophysics.* (1994) **143**:61–87.

[20] Lisitsa V. V., Tcheverda V. A., and Volianskaia V. V. GPU-based implementation of discrete element method for simulation of the geological fault geometry and position. *Supercomputing Frontiers and Innovations.* (2018) **5**:46–50.

[21] Wang Y. and Tonon F. Modeling triaxial test on intact rock using discrete element method with membrane boundary. *Journal of Engineering Mechanics.* (2009) **135**:1029–1037.

[22] Bono J. de, Mcdowell G., and Wanatowski D. Discrete element modelling of a flexible membrane for triaxial testing of granular material at high pressures. *Géotechnique Letters* (2012) **2**:199–203.

[23] Cundall P. A. and Strack O. D. L. A discrete numerical model for granular assemblies. *Géotechnique* (1979) **29**:47–65.

[24] Li Z., Wang Y. H., Ma C. H., and Mok C. M. B. Experimental characterization and 3D DEM simulation of bond breakages in artificially cemented sands with different bond strengths when subjected to triaxial shearing. *Acta Geotechnica* (2017) **12**:987–1002.

[25] Duan K., Kwok C. Y., and Ma X. DEM simulations of sandstone under true triaxial compressive tests. *Acta Geotechnica* (2017) **12**:495–510.

[26] O'Sullivan C., Bray J. D., and Li S. A new approach for calculating strain for particulate media. *International Journal for Numerical and Analytical Methods in Geomechanics.* (2003) **27**:859–877.

[27] Abe S., van Gent H., and Urai J. L. DEM simulation of normal faults in cohesive materials. *Tectonophysics.* (2011) **512**:12–21.

[28] Calinski T. and Harabasz J. A dendrite method for cluster analysis. *Communications in Statistics.* (1974) **3**:1–27.